Magnetic phase diagram of the coupled triangular spin tubes for $CsCrF_4$

Kouichi Seki
Graduate School of Science and Technology, Niigata University, Niigata 950-2181, Japan

Kouichi Okunishi
Department of Physics, Niigata University, Niigata 950-2181, Japan

(Received 23 February 2015; revised manuscript received 10 May 2015; published 2 June 2015)

Using Monte Carlo simulations, we explore the magnetic phase diagram of triangular spin tubes coupled with a ferromagnetic intertube interaction for $CsCrF_4$. The planar structure of the coupled tubes is topologically equivalent to the kagome-triangular lattice, which induces nontrivial frustration effects in the system. We particularly find that, depending on the intertube coupling, various ordered phases are actually realized, such as incommensurate order, ferromagnetic order, and cuboc order, which is characterized by the noncoplanar spin structure of the 12 sublattices accompanying the spin chirality breaking. We also discuss the relevance of the results to recent experiments on $CsCrF_4$.

DOI: 10.1103/PhysRevB.91.224403 PACS number(s): 75.10.Hk, 05.10.Ln, 75.40.Cx

I. INTRODUCTION

Recently, the triangular spin tube has attracted much interest, where its geometrical frustration and quasi-one-dimensionality cooperatively induce exotic magnetic behaviors. Indeed, theoretical investigations of the $S = 1/2$ quantum spin tube [1] have revealed various interesting properties such as a gapful ground state [2–8], field-induced chirality order [9,10], etc. Moreover, extensive theoretical researches have been performed for various quantum spin tubes, such as integer-spin tubes [11], $S = 3/2$ triangular tubes [12,13], and four-leg tubes [14]. Also, the triangular spin tube has been a target of intensive experimental studies. For example, several experiments on $[(CuCl_2tachH)_3Cl]Cl_2$, which is an $S = 1/2$ spin tube consisting of alternating triangles along the tube direction, clarified various characteristic behaviors originating from the tube structure [15,16]. Moreover, the straight-type spin tubes $CsCrF_4$ and α-$KCrF_4$ have been recently synthesized, which are respectively based on equilateral and nonequilateral triangles [17–20]. These compounds interestingly provide essential information about the shape dependence of the unit triangle in spin tubes.

In $CsCrF_4$, Cr^{3+} ions having $S = 3/2$ spin form a rigid equilateral triangular tube (Fig. 1), where dominant exchange couplings are antiferromagnetic and the intertube coupling is estimated to be basically very small. Accordingly, no anomaly associated with a phase transition was observed by bulk measurements and electron spin resonance experiments down to $T = 1.5$ K [18–20]. On the other hand, a recent experiment on the ac susceptibility observed anomalous slow dynamics suggesting a magnetic long-range order below 4 K [21]. In addition, a very recent neutron diffraction experiment suggests that this magnetic order is inconsistent with the naive 120° structure due to the conventional triangle lattice [22]. Thus, it is expected that the equilateral-triangle structure and a small but finite intertube coupling cooperatively induce a nontrivial magnetic structure in $CsCrF_4$, which could be indeterminate in the bulk quantities.

In order to analyze the magnetic structure of $CsCrF_4$, a key observation is that Cr^{3+} has a relatively large spin $S = 3/2$, and a certain spin order is suggested by magnetic diffraction peaks in the neutron experiment [22]. Thus, we can expect that the magnetic order of $CsCrF_4$ is basically described by the classical Heisenberg model defined on the triangular-tube lattice. As depicted in Figs. 1 and 2, moreover, the intertube coupling in the ab plane has the same lattice topology as the kagome-triangular lattice [23], although the exchange coupling along the c axis is dominant in the spin tube. Thus, the lattice structure of $CsCrF_4$ involves a frustration effect even for ferromagnetic intertube coupling.

Of course, the Heisenberg model on the planar lattice has no magnetic long-range order at a finite temperature. In the present coupled tubes, however, the three-dimensional (3D) couplings possibly stabilize a peculiar spin fluctuation originating from the kagome-triangular structure. Using Monte Carlo (MC) simulations, in this paper, we investigate finite-temperature phase transitions of the classical Heisenberg model on triangular spin tubes with intertube interaction. In particular, we find that the 12-sublattice spin structure—cuboc order—in the ab plane emerges in the regime of small ferromagnetic intertube coupling. The cuboc order, which was originally proposed for the ground state of the planar kagome lattice model with next-nearest-neighbor interaction, is characterized by a noncoplanar spin structure with triple $\boldsymbol{q}$ wave vectors [24–26]. In spin tubes, this cuboc order can be stabilized to be 3D long-range order by the strong leg coupling of the tube at a finite temperature. We also discuss the nature of the transitions for the cuboc phase, as well as the incommensurate and ferromagnetic phases, depending on the intertube coupling. Finally we discuss the relevance to the $CsCrF_4$ experiments.

This paper is organized as follows. In Sec. II, we explain details of the model and the possible orders. In Sec. III, we describe details of MC simulations and definitions of order parameters. In Sec. IV, we present results of MC simulations and summarize the phase diagram with respect to the intertube coupling. We also mention universalities of the phase transitions. In Sec. V, we summarize the conclusions and discuss the relevance to the $CsCrF_4$ experiments.

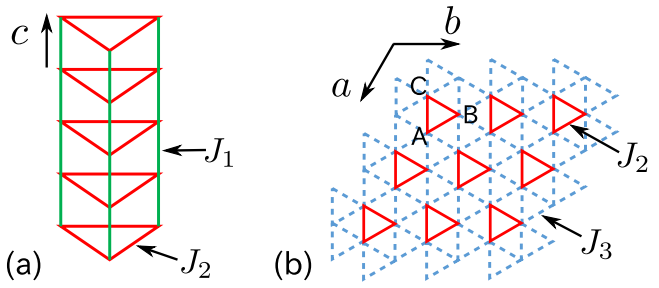

FIG. 1. (Color online) Lattice structure of triangular tubes with an intertube interaction. (a) A triangular spin tube, where J_1 is the dominant antiferromagnetic coupling in the tube direction (c axis) and J_2 denotes the antiferromagnetic interaction in the unit triangle. (b) The lattice structure in the ab plane. The triangles of solid lines correspond to the J_2 coupling in the spin tubes and the triangles of broken lines denote the ferromagnetic intertube interaction J_3.

II. MODEL AND ORDERS

As depicted in Fig. 1, a bundle of triangular spin tubes in $CsCrF_4$ runs in the c-axis direction and these tubes with the intertube coupling cover the triangular lattice in the ab plane. We thus consider the classical Heisenberg model on a stacked triangular lattice, which reads

$$\mathcal{H} = J_1 \sum_{\langle i,k\rangle_c} \boldsymbol{S}(\boldsymbol{r}_i)\cdot\boldsymbol{S}(\boldsymbol{r}_k) + J_2 \sum_{\langle i,j\rangle_\triangle} \boldsymbol{S}(\boldsymbol{r}_i)\cdot\boldsymbol{S}(\boldsymbol{r}_j) + J_3 \sum_{\langle\langle i,j\rangle\rangle} \boldsymbol{S}(\boldsymbol{r}_i)\cdot\boldsymbol{S}(\boldsymbol{r}_j), \quad (1)$$

where $\boldsymbol{r}_i$ represents the position vector of site i, and $\boldsymbol{S}(\boldsymbol{r}_i) = S_i^x\boldsymbol{e}_x + S_i^y\boldsymbol{e}_y + S_i^z\boldsymbol{e}_z$ with $|\boldsymbol{S}_i| = 1$ denoting the vector spin at the ith site. Note that $\boldsymbol{e}_\alpha$ ($\alpha \in x,y,z$) indicates the unit vector in the spin space, while the primitive lattice translation vectors are represented as $\boldsymbol{a}$, $\boldsymbol{b}$, and $\boldsymbol{c}$ with $|\boldsymbol{a}| = |\boldsymbol{b}| = |\boldsymbol{c}| = 1$ (Fig. 1). Moreover, $\langle i,k\rangle_c$ denotes the sum of the nearest-neighbor spins along the c axis, $\langle i,j\rangle_\triangle$ indicates the sum of spin pairs in the unit triangle, and $\langle\langle i,j\rangle\rangle$ runs over spin pairs of the intertube couplings in the ab plane. In this paper, we basically assume the antiferromagnetic interactions $J_1 \geqslant J_2 > 0$ in the spin tube and the ferromagnetic intertube interaction $J_3 < 0$. Note that a local density approximation (LDA) + U calculation gives $J_1/J_2 \simeq 2.0$ and $J_3/J_2 \simeq 0$ with $J_2 \simeq 20$ K for $CsCrF_4$ [27].

In analyzing possible ordering of the coupled-tube model, an important point is that the dominant coupling J_1 along the tube direction does not cause any frustration. Thus, the staggered pattern of the spin order formed in the ab plane is realized in the c-axis direction. This implies that the low-temperature spin structure is essentially attributed to the frustrating interactions in the ab plane, which we will actually justify with MC simulations in the next section. In the following, we therefore assume staggered order in the c-axis direction, and concentrate on the spin structure in the ab plane.

As in Fig. 2(a), the planar structure of the model is topologically equivalent to the kagome-triangular lattice, where J_3 corresponds to the nearest-neighbor coupling competing with the next-nearest-neighbor interaction J_2 [23]. Then a candidate for the ground-state order is classified by Fourier transformation of the Hamiltonian. Defining the unit cell as a triangle of the J_2 coupling, we have

$$\mathcal{H} = \frac{1}{2}\sum J_{\alpha\beta}(\boldsymbol{q})\boldsymbol{S}_{-\boldsymbol{q},\alpha}\cdot\boldsymbol{S}_{\boldsymbol{q},\beta}, \quad (2)$$

where $\boldsymbol{S}_{\boldsymbol{q},\alpha} \equiv \frac{1}{\sqrt{N}}\sum_{\boldsymbol{r}} e^{-i\boldsymbol{q}\cdot\boldsymbol{r}}\boldsymbol{S}_\alpha(\boldsymbol{r})$. Here, $\boldsymbol{r}$ represents the position of a unit triangle, $\alpha \in \{A,B,C\}$ indicates the sublattice index in the unit triangle, and N is the total number of unit triangles in the system. In addition, $J_{\alpha\beta}(\boldsymbol{q}) \equiv \sum_{\alpha,\beta} e^{-i\boldsymbol{q}\cdot\boldsymbol{r}_{\alpha\beta}} J_{\alpha\beta}$, where $\boldsymbol{r}_{\alpha\beta}$ and $J_{\alpha\beta}$ respectively denote the relative vector of a spin pair and the corresponding coupling associated with spins in the unit cell. Note that the wave vector $\boldsymbol{q}$ runs over the first Brillouin zone in the ab plane. By determining the lowest-energy state of $J_{\alpha\beta}(\boldsymbol{q})$, we have the ground-state phase diagram of Eq. (1) in the J_2-J_3 plane [Fig. 2(b)], which is equivalent to that obtained in Ref. [23].

In Fig. 2(b), $CsCrF_4$ is located near $J_3 \simeq 0$ and $J_2 > 0$. If J_3 is antiferromagnetic, Eq. (1) is a triangular-lattice antiferromagnet for which the ground state is the 120° structure. However, the neutron diffraction experiment suggested that the order of $CsCrF_4$ is not explained by a naive 120° structure [22]. We thus discuss the negative J_3 (<0) region, where the nontrivial exotic order phase actually emerges; In the $-J_3 \leqslant J_2$ region, particularly, the minimum of $J_{\alpha\beta}(\boldsymbol{q})$ located at the M point in the Brillouin zone, where the noncoplanar order with the 12 sublattices that is called "cuboc" order can be stabilized. As $-J_3$ increases, the incommensurate order appears in the $J_2 < -J_3 < 2J_2$ region, and finally the ferromagnetic order becomes stable for $-J_3 \geqslant 2J_2$. This ground-state phase diagram suggests that, in $CsCrF_4$, the cuboc state can be stabilized to be the 3D long-range order at a finite temperature by the tube-leg coupling J_1, even if the amplitude of the intertube interaction J_3 is very small.

Here, we briefly summarize the essential property of the cuboc order in $0 < -J_3 < J_2$, which was originally found in the J_1-J_2 Heisenberg model on the kagome lattice [24–26]. The cuboc order has a noncoplanar spin structure accompanying the spontaneous symmetry breaking of the lattice translation. Figure 3(a) shows the extended unit cell for the cuboc order in the ab plane, where we assign a number to each of four triangles, for later convenience. Then the strong antiferromagnetic coupling J_2 basically imposes the 120°

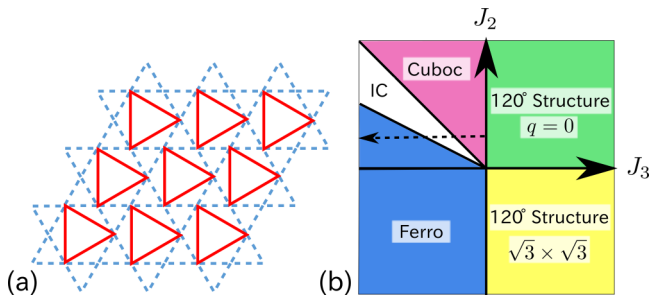

FIG. 2. (Color online) (a) Topology of the coupled-spin-tube lattice in the ab plane, equivalent to that of the kagome-triangular lattice. (b) The ground-state phase diagram of the classical Heisenberg model on the coupled triangular spin tubes. The left-going dashed arrow shows the direction of the J_3 parameter corresponding to the finite-temperature phase diagram in Sec. IV.

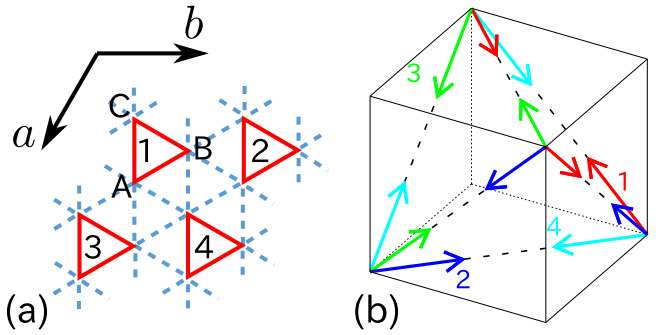

FIG. 3. (Color online) (a) The extended unit cell for the cuboc order with the 12-sublattice structure. The label $\{A,B,C\}$ indicates each vertex in the unit triangle and the number $\{1,2,3,4\}$ represents the label of a triangle in the extended unit cell. (b) The arrow with the numbers shows the spin directions forming the 120° structure in the corresponding unit triangle. The four tilting 120° structures in the extended unit cell form the tetrahedron represented by the dashed lines.

structure in each triangle. A significant point is that the 120°-structure planes can have a relative tilt among the four triangles, so as to reduce the energy due to the frustrating J_3 interaction. Gluing together the four tilting triangles of the 120° structure, we obtain a tetrahedron where the 12 spins in the extended unit cell are attached. As shown in Fig. 3(b), the three spins on the unit triangle of the original lattice are mapped into the vertices of the corresponding triangle on the tetrahedron, where the vector-spin chiralities existing on the four 120° planes point in the radial direction from the center of the tetrahedron. In this sense, the vector-spin chirality associated with the tetrahedron can be a good order parameter for the noncoplanar cuboc spin structure. Note that, if the spin vectors are arranged at the origin of the spin space, we have the same schematic diagram as in Refs. [24–26].

For the cuboc order, the magnetic propagation vectors interestingly have a triple-$\boldsymbol{q}$ structure in the ab plane, reflecting the above characteristic spin configuration. Let us write the sublattice spin in the unit cell at position $\boldsymbol{r}$ as $\boldsymbol{S}_\alpha(\boldsymbol{r})$, where $\alpha \in \{A,B,C\}$ is the sublattice index in the unit triangle. Then the cuboc order can be explicitly written as

$$\begin{aligned}
\boldsymbol{S}_A(\boldsymbol{r}) &= \cos\left(\frac{1}{2}\boldsymbol{q}_a\cdot\boldsymbol{r}\right)\frac{\boldsymbol{e}_x}{\sqrt{2}} - \cos\left(\frac{1}{2}\boldsymbol{q}_\gamma\cdot\boldsymbol{r}\right)\frac{\boldsymbol{e}_y}{\sqrt{2}},\\
\boldsymbol{S}_B(\boldsymbol{r}) &= \cos\left(\frac{1}{2}\boldsymbol{q}_\gamma\cdot\boldsymbol{r}\right)\frac{\boldsymbol{e}_y}{\sqrt{2}} - \cos\left(\frac{1}{2}\boldsymbol{q}_b\cdot\boldsymbol{r}\right)\frac{\boldsymbol{e}_z}{\sqrt{2}},\\
\boldsymbol{S}_C(\boldsymbol{r}) &= \cos\left(\frac{1}{2}\boldsymbol{q}_b\cdot\boldsymbol{r}\right)\frac{\boldsymbol{e}_z}{\sqrt{2}} - \cos\left(\frac{1}{2}\boldsymbol{q}_a\cdot\boldsymbol{r}\right)\frac{\boldsymbol{e}_x}{\sqrt{2}},
\end{aligned} \tag{3}$$

where $\boldsymbol{q}_a,\boldsymbol{q}_b$ are the reciprocal lattice vectors of the primitive translation vectors $\boldsymbol{a},\boldsymbol{b}$, and $\boldsymbol{q}_\gamma \equiv \boldsymbol{q}_a - \boldsymbol{q}_b$. This triple $\boldsymbol{q}$ is an important feature of the cuboc phase and plays an essential role in the analysis of the neutron diffraction experiment. Finally, we note that, in the c-axis direction, the magnetic propagation vector is $\boldsymbol{q}_c/2$, where a simple staggered pattern appears.

III. MONTE CARLO SIMULATION

In the previous section, we discussed the ground-state orders of the triangular spin tubes in the ab plane for $-J_3 \leqslant J_2$. So far, investigations of the planar kagome-triangular-lattice model have clarified that, although there exists no true long-range order of the spin, the chirality degrees of freedom associated with the cuboc order induce a Z_2-symmetry-breaking transition even at a finite temperature [24,25]. For the coupled-tube system, which contains the full 3D couplings, we can expect the finite-temperature transitions associated with cuboc long-range order, incommensurate order, as well as ferromagnetic order. In order to address the nature of these finite-temperature transitions, we perform extensive Monte Carlo simulations for the coupled-tube system of Eq. (1).

Here, we comment on the notation for the system size. In the following, we basically represent the linear dimensions of the system by the number of triangles associated with J_2 couplings. Thus, L_a (L_b) means the number of triangles in the a- (b-) axis direction, and L_c denotes the length of a tube in the c-axis direction. In this paper, we basically deal with the system of $L_a = L_b = L_c \equiv L$, for which the total number of spins in the system is $N = 3L^3$.

A. Details of the simulation

We employ Wolff's cluster algorithm [28] combined with the Metropolis local update. Usually, the Wolff algorithm is not efficient for frustrated systems, where a large cluster containing almost all of the spins is often generated. However, we find that the coupled spin tubes have no frustration in the c axis, which makes possible cluster growth of an efficient size in the tube direction. Thus the Wolff algorithm works very well for the coupled spin tubes. Note that the parallel tempering method [29] is additionally used in practical computations, if the relaxation to equilibrium is difficult. On the basis of the above algorithm, we performed MC simulations for systems of size $L = 8,16,\ldots,36$ with periodic boundary conditions. We particularly explore the T-J_3 phase diagram along the dashed arrow in Fig. 2(b) with $J_2 = 1.0$ fixed. Typical numbers of MC samples are 2^{19}–2^{23}.

B. Order parameters

As pointed out in the ground-state phase diagram of Fig. 2(b), the coupled triangular spin tubes have various ordered states. To classify these ordered states in simulations, we need to define appropriate order parameters. In particular, the cuboc order has a noncoplanar spin structure with 12 sublattices in the ab plane, which is stacked in a staggered fashion in the c-axis direction. Taking account of this structure, we define the cuboc sublattice magnetization $\boldsymbol{m}_{\alpha,\beta}$ in a certain ab plane, where $\alpha \in \{A,B,C\}$ indicates a vertex of a triangle, and $\beta \in \{1,2,3,4\}$ specifies a triangle in the extended unit cell [Fig. 3(a)],

$$\boldsymbol{m}_{\alpha,\beta} \equiv \frac{1}{N_p}\sum_{\boldsymbol{r}_\beta}{}' \boldsymbol{S}_\alpha(\boldsymbol{r}_\beta), \tag{4}$$

where $\boldsymbol{r}_\beta$ denotes the position of the triangle labeled by β in the extended unit cell, and $\sum'_{\boldsymbol{r}_\beta}$ represents the sum with

respect to triangles having the same α in the plane. In addition, the normalization $N_p \equiv L^2/4$ is the number of extended unit cells in the ab plane. Then the sublattice magnetization order parameter in the entire system is defined as

$$\boldsymbol{M}_{\alpha,\beta} \equiv \frac{1}{L}\sum_{i_c}(-1)^{i_c}\boldsymbol{m}_{\alpha,\beta}, \tag{5}$$

where i_c denotes the index of the tube direction [Fig. 1(a)].

In the $-J_3 > 2J_2$ region, the ground state of the system is the ferromagnetic ordered state in a certain kagome-triangular plane. Thus, we also introduce the ferromagnetic order parameter as

$$\boldsymbol{m}_F \equiv \frac{1}{12}\sum_{\alpha,\beta}\boldsymbol{m}_{\alpha,\beta}, \tag{6}$$

which detects the uniform magnetization in a kagome-triangular plane. Then this in-plane ferromagnetic order is tacked in a staggered way in the c-axis direction. Thus we define the total ferromagnetic order parameter $\boldsymbol{M}_F$ as

$$\boldsymbol{M}_F \equiv \frac{1}{L}\sum_{i_c}(-1)^{i_c}\boldsymbol{m}_F. \tag{7}$$

Cuboc order is basically detectable by the 12-sublattice magnetization $\boldsymbol{M}_{\alpha\beta}$. As was mentioned in the previous section, moreover, there is another essential order parameter—the chirality degrees of freedom—originating from the 120° structure on the unit triangle. For the unit triangle at $\boldsymbol{r}$, we define the vector-spin chirality [30],

$$\boldsymbol{\kappa}(\boldsymbol{r}) \equiv \frac{2}{3\sqrt{3}}\left[\boldsymbol{S}_A(\boldsymbol{r})\times\boldsymbol{S}_B(\boldsymbol{r}) + \boldsymbol{S}_B(\boldsymbol{r})\times\boldsymbol{S}_C(\boldsymbol{r}) + \boldsymbol{S}_C(\boldsymbol{r})\times\boldsymbol{S}_A(\boldsymbol{r})\right]. \tag{8}$$

An important point about the cuboc order is that the vector chiralities associated with the four triangles in the extended unit cell also have noncoplanar configuration. Thus, we introduce the sublattice vector-chirality order parameter for the cuboc state as

$$\boldsymbol{K}_\beta \equiv \frac{1}{LN_p}\sum_{i_c}\sum_{\boldsymbol{r}_\beta}{}'\boldsymbol{\kappa}(\boldsymbol{r}_\beta), \tag{9}$$

where $\sum'_{\boldsymbol{r}_\beta}$ sums over $\boldsymbol{\kappa}$ carrying the sublattice index β of the extended unit cell. Here, note that the vector-spin chirality takes the same sign in the c-axis direction, although the directions of the spins are alternately aligned.

In the cuboc phase, both $\boldsymbol{M}_{\alpha,\beta}$ and $\boldsymbol{K}_\beta$ have finite values, but $\boldsymbol{M}_F = \boldsymbol{0}$. In the ferromagnetic state, $\boldsymbol{M}_F$ is finite, while $\boldsymbol{K}_\beta = \boldsymbol{0}$. For the incommensurate phase between the cuboc and ferromagnetic phases, we do not set up a direct order parameter of the incommensurate spin configuration, because it is very difficult to determine the pitch of the incommensurate oscillation within a system size up to $L = 36$. However, it should be noted that $\boldsymbol{M}_{\alpha,\beta} = \boldsymbol{0}$ and $\boldsymbol{K}_\beta = \boldsymbol{0}$ are basically seen in the incommensurate phase.

IV. RESULTS

We present results of MC simulations for typical parameters of the coupled spin tubes. As mentioned in Sec. II, the parameters corresponding to $CsCrF_4$ are that $J_1/J_2 \simeq 2$ and $J_3/J_2 \simeq 0$. In this paper, we fix $J_2 = 1.0$ and investigate the intertube-coupling (J_3) dependence for $J_1 = 1.0$ and 3.0, along the dashed arrow in the ground-state phase diagram in Fig. 2(b). We then find no qualitative difference between $J_1 = 1.0$ and 3.0, so that we show the results for $J_1 = 1.0$ below.

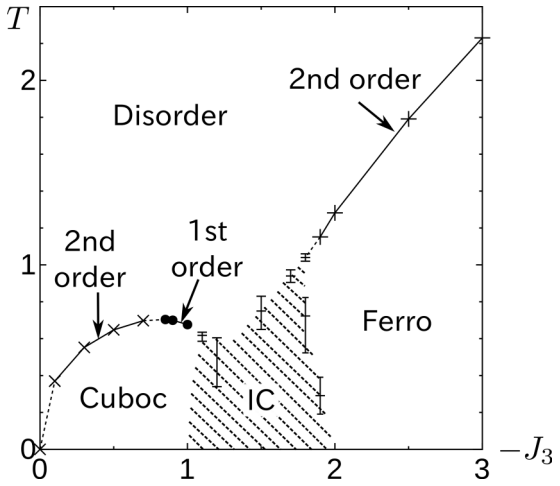

FIG. 4. T-J_3 phase diagram of the coupled triangular spin tubes with $J_1 = J_2 = 1.0$. Cuboc order is realized at finite temperature by intertube interaction.

A. Phase diagram

In Fig. 4, we show the final phase diagram in the T-J_3 plane, before presenting a detailed analysis of the simulations. Note that the horizontal axis represents $-J_3$, since we consider the negative-J_3 region. In the figure, it is verified that the long-range orders at a finite temperature are consistent with the ground-state phase diagram of the planar kagome-triangular model in Fig. 2. For $0 < -J_3 \lesssim 1$, the cuboc phase is actually realized, and, in $1 \lesssim -J_3 \lesssim 2$, incommensurate spin order appears. Moreover, the system exhibits ferromagnetic order for $-J_3 \gtrsim 2$, where the ferromagnetic coupling is dominant.

The phase boundary of the cuboc-disorder transition is of second order for $-J_3 \lesssim 0.7$, which can be determined with a finite-size-scaling analysis. The universality of this second-order-transition line is associated with the triple-$\boldsymbol{q}$ structure of the cuboc order, and it is possibly different from such a well-known universality as layered triangular lattice. A detailed scaling analysis will be presented in the following section. For $0.85 \lesssim -J_3 \lesssim 1.1$, however, the cuboc-disorder transition changes to first order, where a double peak of the energy histogram is observed. Note that a precise identification of the transition is difficult around $-J_3 \sim 0.8$, where a tricritical point is expected. For $1.1 \lesssim -J_3 \lesssim 1.8$, the incommensurate-disorder transition line is estimated by the peak position of the specific heat within finite-size systems up to $L = 32$, where size extrapolation is difficult. For $-J_3 \gtrsim 1.8$, the line of the disorder-ferromagnetic order transition is of second order, for which the universality class is consistent with the 3D ferromagnetic Heisenberg model. On the other hand, the transitions between the incommensurate phase and the other ordered phases are expected to be of commensurate-

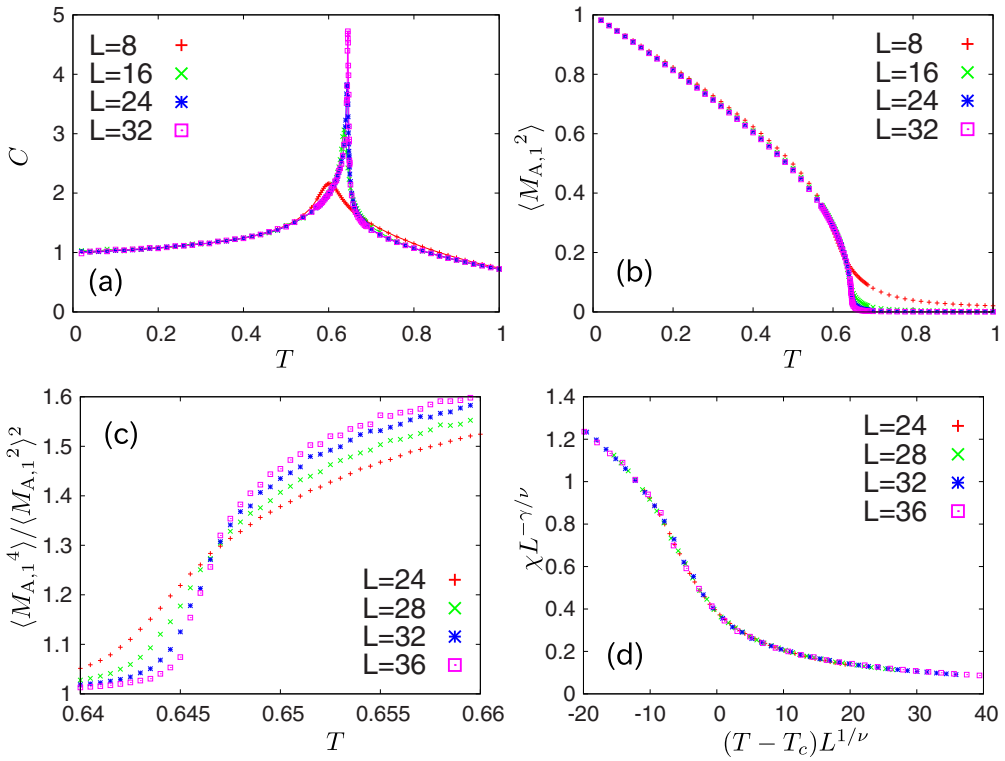

FIG. 5. (Color online) Results of MC simulations for $-J_3 = 0.5$. (a) Specific heat C. (b) Mean-square average of the cuboc sublattice magnetization $\langle \boldsymbol{M}_{A,1}^2 \rangle$. (c) Binder cumulant for $\boldsymbol{M}_{A,1}$. (d) Finite-size-scaling plot for the cuboc order parameter, which yields $T_c = 0.647\,21(4)$, $\nu = 0.435(4)$, and $\gamma = 0.90(2)$.

incommensurate type. These transition lines associated with the incommensurate order are also estimated within finite-size results.

B. Cuboc phase

Let us begin with a detailed analysis of the cuboc phase. In Figs. 5 and 6, we present MC results for the cuboc phase. The specific heat C and the mean-square average of the cuboc sublattice magnetization $\langle \boldsymbol{M}_{A,1}^2 \rangle$ are shown in Figs. 5(a) and 5(b). First of all, the specific heat C has a sharp single peak at $T_c \sim 0.65$, and the sublattice magnetization $\boldsymbol{M}_{A,1}$ also exhibits the phase transition behavior at the same temperature. In order to precisely determine the transition point, we calculate the Binder cumulant [31] of the cuboc sublattice magnetization $\langle \boldsymbol{M}_{A,1}^4 \rangle / \langle \boldsymbol{M}_{A,1}^2 \rangle^2$. The result for $-J_3 = 0.5$ is shown in Fig. 5(c), where the curves for various system sizes cross at $T_c = 0.6470(5)$. This implies that the transition is of second order, prompting us to determine the universality class of the cuboc transition with a finite-size-scaling analysis. Assuming the scaling form for the susceptibility of the cuboc sublattice magnetization,

$$\chi \equiv L N_p \langle \boldsymbol{M}_{A,1}^2 \rangle / T \propto L^{\gamma/\nu} \Psi(t L^{1/\nu}) \tag{10}$$

with $t = (T - T_c)/T_c$, we perform a Bayesian estimation for the critical exponents ν, γ, and T_c [32]. Figure 5(d) shows the resulting finite-size-scaling plot for χ with the best-fit values $\nu = 0.435(4)$, $\gamma = 0.90(2)$, and $T_c = 0.647\,21(4)$. Here, we note that T_c is consistent with the result of the Binder cumulant, although it is obtained independently of the Binder-cumulant result. Taking account of the error originating from the choice of the data window, we finally adopt $\nu = 0.44(2)$ and $\gamma = 0.91(3)$ for the critical exponents of the cuboc sublattice magnetization.

As mentioned before, the sublattice vector-spin chirality is also another essential order parameter of the cuboc order. Figure 6(a) shows $\langle \boldsymbol{K}_1^2 \rangle$ for $-J_3 = 0.5$, where the transition occurs at the same T_c as for the sublattice magnetization $\boldsymbol{M}_{A,1}$. This behavior is consistent with the observation that the specific heat has a single peak at T_c. Thus, we can expect that the cuboc magnetization and the chirality degrees of freedom exhibit a simultaneous transition. We then perform a finite-size-scaling analysis for the chirality susceptibility with $\chi_K \equiv L N_p \langle \boldsymbol{K}_1{}^2 \rangle / T \propto L^{\gamma_K/\nu} \Psi_K(t L^{1/\nu})$. In Fig. 6(b), we present the finite-size-scaling plot with $T_c = 0.647\,42(4)$, $\nu = 0.433(8)$, and $\gamma_K = 0.57(2)$, which are also obtained with the Bayesian estimation [32]. Taking account of the data-window dependence, we finally identify the exponents associated with the vector-spin chirality as $\nu = 0.43(2)$ and $\gamma_K = 0.55(4)$. Here, it should be noted that, although no *a priori* assumption on T_c and ν was set up in this scaling analysis, the resulting T_c and ν are consistent with those for χ, while γ_K is clearly different from γ. These facts suggest that the singular part of the free energy scales with

$$f_s \propto L^{-d} f_s(t L^{1/\nu}, h L^{y}, h_K L^{y_K}), \tag{11}$$

where y [$= (\frac{\gamma}{\nu} + d)/2$] and y_K [$= (\frac{\gamma_K}{\nu} + d)/2$] are the eigenvalues of the linearized renormalization-group transformation corresponding to the fields conjugated to the cuboc magnetization and the chirality, respectively. Thus we have concluded

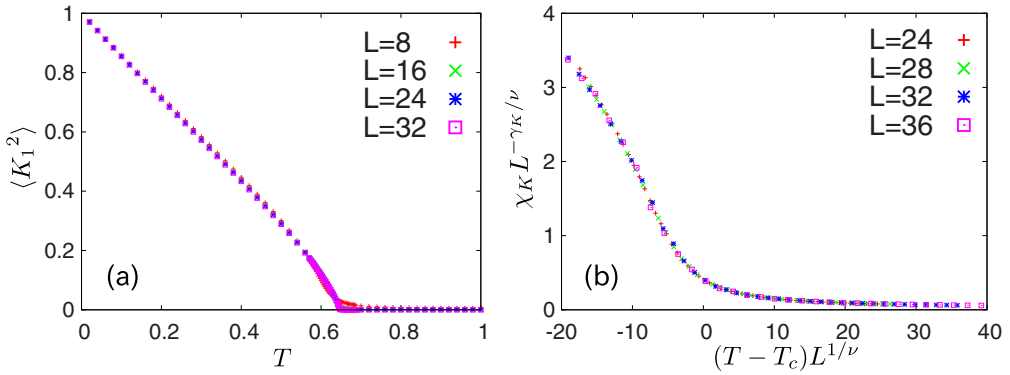

FIG. 6. (Color online) Results of the vector-spin chirality for $-J_3 = 0.5$. (a) Mean-square average of the sublattice vector-spin chirality $\langle \boldsymbol{K}_1^2 \rangle$. (b) Finite-size-scaling plot for $\langle \boldsymbol{K}_1^2 \rangle$, which yields best-fit values $T_c = 0.647\,2(4)$, $\nu = 0.433(8)$, and $\gamma_K = 0.57(2)$.

that the transition of the spin and chirality degrees of freedom is simultaneous. Here, the exponents obtained for the cuboc transition are clearly different from those of the layered triangular-lattice antiferromagnet, although a simultaneous transition was also observed [33–36]. The universality of the cuboc transition might be characterized by an effective chiral Ginzburg-Landau-Wilson theory associated with the triple-$\boldsymbol{q}$ structure [35,37,38]. However, the detailed analysis of the effective model is an interesting future issue. Here, we remark that $\boldsymbol{M}_{\alpha,\beta}$ and $\boldsymbol{K}_\beta$ are confirmed to be consistent among the all combinations of sublattice indices α and β. On the basis of the analysis above, we have finally drawn the second-order-transition line of the cuboc phase in Fig. 4.

We turn to the first-order transition in the region of $0.85 \lesssim -J_3 \lesssim 1.1$. Figure 7 shows MC results for $-J_3 = 1.0$. In Fig. 7(a), the specific heat C also has a sharp single peak at $T_c \sim 0.675$. In Figs. 7(b) and 7(c), moreover, we can observe that mean-square averages of the cuboc sublattice magnetization $\langle \boldsymbol{M}_{A,1}^2 \rangle$ and of the vector-spin chirality $\langle \boldsymbol{K}_1^2 \rangle$ also exhibit the phase transition behavior at the same temperature T_c, illustrating the simultaneous transition of the spin and chirality degrees of freedom. In the figures, we can also observe that both of $\langle \boldsymbol{M}_{A,1}^2 \rangle$ and $\langle \boldsymbol{K}_1^2 \rangle$ for $L = 24$ and 32 show small jumps at T_c, suggesting that the transition is of first order. We have computed the energy histogram around T_c to confirm its double-peak structure at $T_c = 0.675$ [Fig. 7(d)]. Thus, we

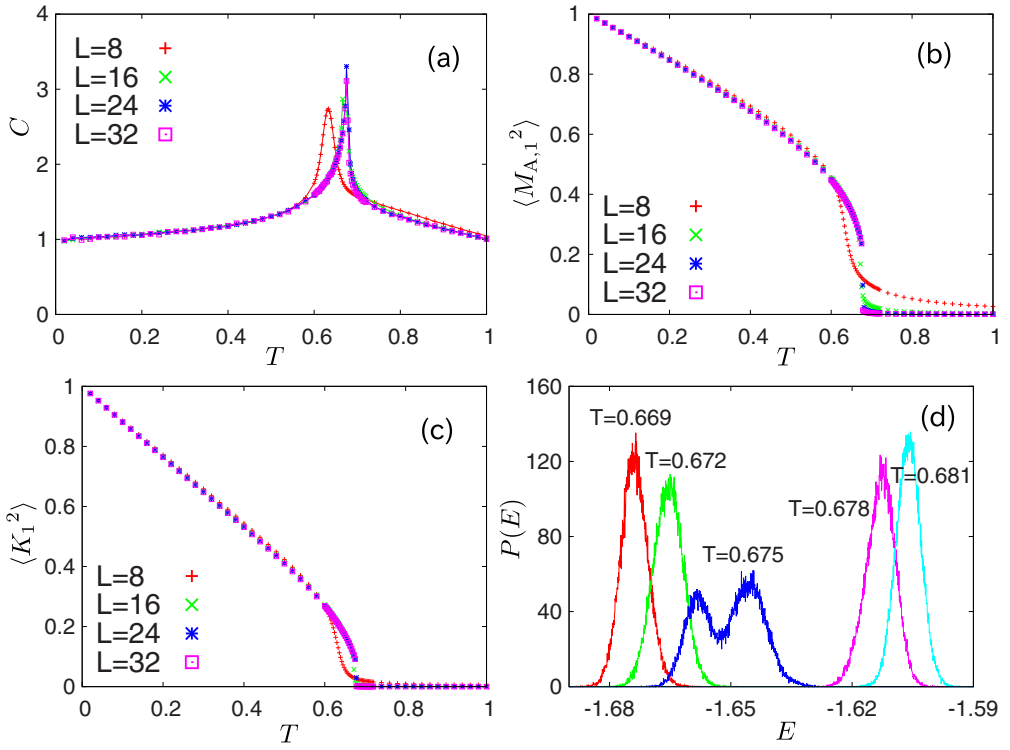

FIG. 7. (Color online) Results of MC simulations at $-J_3 = 1.0$. (a) Specific heat C. (b) Mean-square average of the cuboc sublattice magnetization $\langle \boldsymbol{M}_{A,1}^2 \rangle$. (c) Mean-square average of the sublattice vector-spin chirality $\langle \boldsymbol{K}_1^2 \rangle$. (d) Energy histogram around the transition point for $L = 32$. The double-peak structure emerges at $T_c = 0.675$, indicating that the transition is of first order.

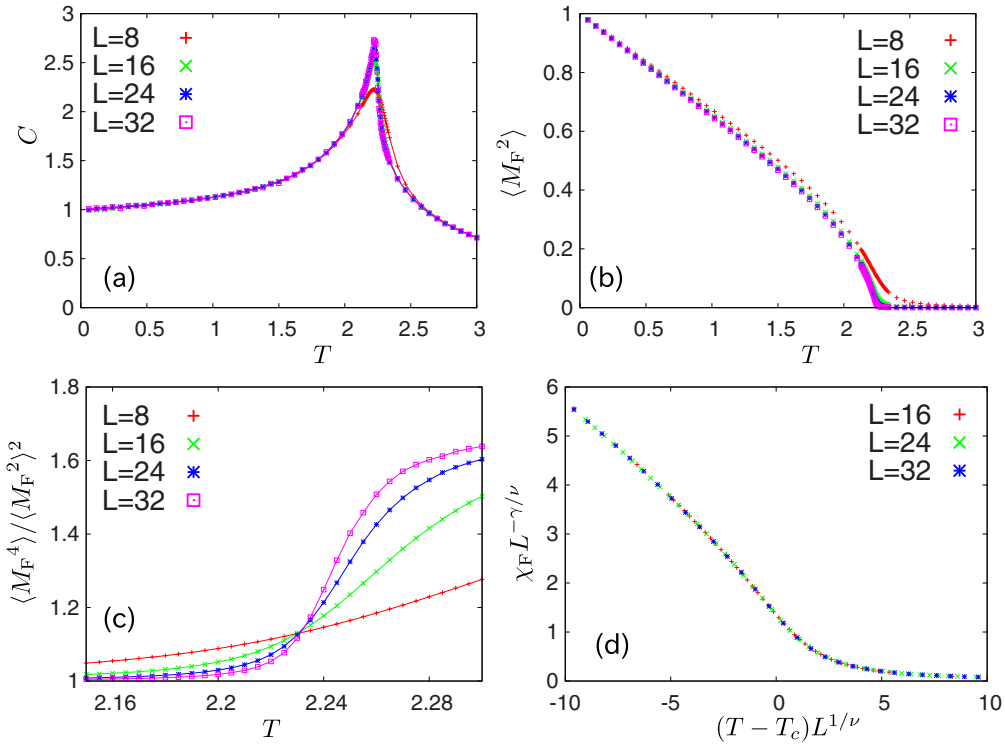

FIG. 8. (Color online) Results for $-J_3 = 3.0$. (a) Specific heat C. (b) Mean-square average of the uniform magnetization $\langle \boldsymbol{M}_F^2 \rangle$. (c) Binder cumulant for $\boldsymbol{M}_F$. (d) Finite-size-scaling plot for the susceptibility of χ_F. The fitting result is consistent with the 3D Heisenberg universality class [39–42].

conclude that the transition in $0.85 \lesssim -J_3 \lesssim 1.1$ is of first order.

Finally, we would like to comment on the tricritical point expected around $-J_3 \sim 0.8$. On varying J_3, we have checked that the double peak of the energy histogram appears down to $-J_3 = 0.85$, while the crossing point of the Binder cumulant emerges up to $-J_3 = 0.7$. Thus, the tricritical point is possibly located around $-J_3 \sim 0.8$. Within the present system size of the MC simulation, however, a precise identification of the tricritical point is difficult. The detailed analysis of this respect is a future issue.

C. Ferromagnetic phase

In the $-J_3 \gtrsim 2.0$ region, the ferromagnetic coupling becomes dominant, and the system forms ferromagnetic order in a kagome-triangular layer, accompanying the second-order phase transition. In Fig. 8, we show results of MC simulations at $-J_3 = 3.0$. The specific heat C in Fig. 8(a) indicates a peak at $T_c \sim 2.2$, and the magnetization $\langle \boldsymbol{M}_F^2 \rangle$ in Fig. 8(b) also exhibits the phase transition behavior. Note that the sublattice spin chirality $\langle \boldsymbol{K}_1^2 \rangle$ is checked to be always zero in the region of the ferromagnetic phase.

In order to precisely determine T_c, we further calculate the Binder cumulant $\langle \boldsymbol{M}_F^4 \rangle / \langle \boldsymbol{M}_F^2 \rangle^2$. The result is shown in Fig. 8(c), where the crossing point appears at $T_c = 2.233(3)$. We also perform a finite-size-scaling analysis of the susceptibility $\chi_F \equiv 12LN_p \langle \boldsymbol{M}_F^2 \rangle / T$, using the Bayesian estimation. The finite-size-scaling plot in Fig. 8(d) collapses well to a scaling function with $T_c = 2.235(5)$, $\nu = 0.70(2)$, and $\gamma = 1.40(5)$. Note that these exponents are clearly consistent with the 3D ferromagnetic Heisenberg class: $\nu \simeq 0.71$ and $\gamma \simeq 1.40$ [39–42]. Thus, we can conclude that the universality class of the transition for the ferromagnetic order is the conventional 3D ferromagnetic Heisenberg class.

D. Incommensurate phase

Let us finally discuss the incommensurate phase in the $1.1 \lesssim -J_3 \lesssim 2$ region, which is sandwiched between the cuboc and ferromagnetic phases. In Fig. 9(a), we show the specific heat C at $-J_3 = 1.5$, where a phase transition is illustrated by a rounded peak of C around $T_c \sim 0.7$. However, a size extrapolation to extract the bulk behavior is usually difficult for incommensurate order, where the pitch of the oscillation does not match the system size. Thus, we basically estimate the transition temperature by the peak position of the specific heat at $L = 32$.

Turning to the transition line between the incommensurate and ferromagnetic phases, we can expect a commensurate-incommensurate type of transition, where the wave vector of the order may continuously sift from the Γ point toward the M point, following the ground-state phase diagram in Fig. 2(b). Figure 9(b) shows the uniform magnetization $\langle \boldsymbol{M}_F^2 \rangle$ for $-J_3 = 1.9$, where we observe that it takes a finite value in $0.35 \lesssim T \lesssim 1.2$, but rapidly decays below $T \sim 0.35$. This behavior indicates that ferromagnetic order appears in the range $0.35 \lesssim T \lesssim 1.2$, but it abruptly changes into incommensurate order in the low-temperature region of $T \lesssim 0.35$. We thus define the boundary between ferromagnetic and incommensurate phases as the middle point of the onset and offset of $\langle \boldsymbol{M}_F^2 \rangle$ for $L = 32$.

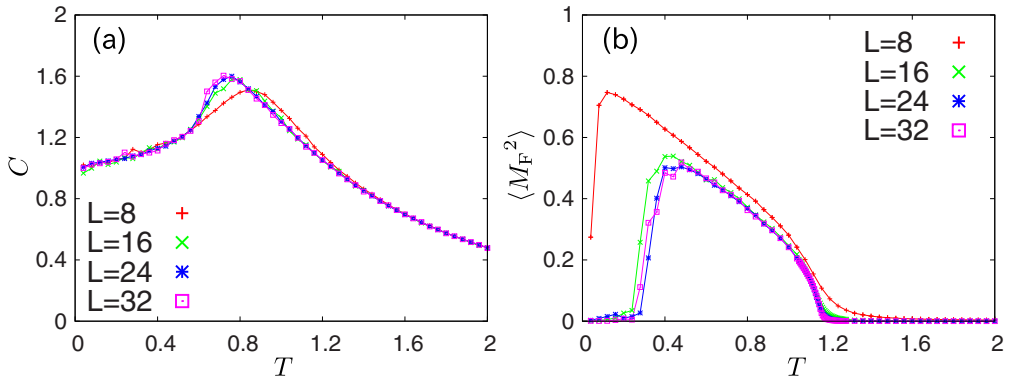

FIG. 9. (Color online) Results of MC simulations for the incommensurate phase. (a) Specific heat C for $-J_3 = 1.5$, which shows a rounded peak at $T \sim 0.7$. (b) Mean-square average of the ferromagnetic magnetization $\langle \boldsymbol{M}_F^2 \rangle$ at $-J_3 = 1.9$, which abruptly decays in the incommensurate order region.

On the other hand, we note that the transition line between the incommensurate and cuboc phases is difficult to estimate from the result within $L = 32$. Thus, the border between the incommensurate and cuboc phases in Fig. 4 is just a guide for eyes.

V. SUMMARY AND DISCUSSION

In this paper, we have investigated phase transitions of the coupled triangular spin tubes associated with $CsCrF_4$. An essential point is that a two-dimensional section of the coupled tubes forms a kagome-triangular plane, which drives the system into exotic orders such as cuboc order, incommensurate order, and ferromagnetic order. In particular, the cuboc order is characterized by the 12-sublattice noncoplanar spin structure carrying triple $\boldsymbol{q}$ wave vectors, which accompanies the noncoplanar structure of the vector-spin chirality as well. Performing extensive Monte Carlo simulations, we have demonstrated that these phases are actually realized for the coupled tubes with negative intertube coupling J_3 at a finite temperature. The resulting phase diagram was summarized in Fig. 4. Then, a particular finding is that the transition to the cuboc order in $-J_3 \lesssim 0.7$ is described by the simultaneous second-order transition of the spin and chirality degrees of freedom. The universality of this transition might be characterized by a noncoplanar spin structure accompanying the chirality, which might be described by an effective chiral Ginzburg-Landau-Wilson theory associated with the triple-$\boldsymbol{q}$ structure [35,37,38]. For $0.85 \lesssim -J_3 \lesssim 1.1$, the transition is of first order, where the double peak of the energy histogram is confirmed. However, the analysis of the expected tricritical point is a remaining issue. On the other hand, for $-J_3 \gtrsim 1.9$, we have confirmed that the ferromagnetic transition belongs to the 3D Heisenberg universality class.

From the experimental view point, $CsCrF_4$ is described by the weak-J_3-coupling limit of the present model. A neutron scattering experiment on $CsCrF_4$ actually suggests that a possible spin order is not the naive 120° structure [22], and thus a finite-temperature transition to the cuboc phase can be expected. However, we should also take account of another fact: a specific-heat experiment on $CsCrF_4$ captures no anomaly down to 1.5 K, while the bulk phase transition to the cuboc phase should theoretically be accompanied by a certain anomaly of the specific heat. A reason for this inconsistency is an anisotropic interaction effect. Since the intertube coupling J_3 of $CsCrF_4$ is basically very small, the Dzyaloshinsky-Moriya interaction [43,44], which is actually suggested in $CsCrF_4$ due to its crystal structure [19], can compete with the small J_3 coupling. Then, such an anisotropy effect may affect the cuboc order configuration, and a transition with a small-scale anomaly could be easily modified into a weak crossover. A direct comparison of the neutron scattering experiment of $CsCrF_4$ with the cuboc order is highly desirable. In addition to the above, we should also analyze how the quantum fluctuation affects the stability of the cuboc order, which is another significant problem to understand the $CsCrF_4$ experiment.

In this paper, we have basically investigated the strong-leg-coupling region ($J_1 \geqslant J_2 \gg |J_3|$), since our motivation is in the spin tube system. Our result implies that the leg coupling certainly stabilizes the cuboc order to be a true long-range order with a simultaneous transition of the spin and chirality. On the other hand, the cuboc order was originally proposed for the planar kagome model with next-nearest-neighbor coupling, where the spin and Z_2 chirality transitions are separated [24,25]. Recently, a cuboc-type spin fluctuation was actually suggested for kapellasite, which may be described by an $S = 1/2$ kagome antiferromagnet containing up to third-nearest-neighbor couplings [45]. Theoretical investigations stimulated by kapellasite also have revealed interesting properties attributed to the kagome structure [46–49]. Thus, it is an essential problem to understand how the 3D cuboc class can be connected to the spin-liquid-like behavior with Z_2 chirality breaking in the limit of the planar kagome-triangular model.

ACKNOWLEDGMENTS

The authors would like to thank T. Okubo and K. Harada for fruitful discussions and comments. They are also grateful to H. Manaka, T. Masuda, and M. Hagihara for discussions about experiments on $CsCrF_4$. This work was supported in part by Grants-in-Aid No. 26400387 and No. 23340109 from the Ministry of Education, Culture, Sports, Science and Technology of Japan.

[1] T. Sakai, M. Sato, K. Okamoto, K. Okunishi, and C. Itoi, J. Phys.: Condens. Matter **22**, 403201 (2010).
[2] K. Kawano and M. Takahashi, J. Phys. Soc. Jpn. **66**, 4001 (1997).
[3] D. C. Cabra, A. Honecker, and P. Pujol, Phys. Rev. B **58**, 6241 (1998).
[4] K. Okunishi, S. Yoshikawa, T. Sakai, and S. Miyashita, Prog. Theor. Phys. Suppl. **159**, 297 (2005).
[5] J.-B. Fouet, A. Läuchli, S. Pilgram, R. M. Noack, and F. Mila, Phy. Rev. B **73**, 014409 (2006).
[6] S. Nishimoto and M. Arikawa, Phys. Rev. B **78**, 054421 (2008).
[7] T. Sakai, M. Sato, K. Okunishi, Y. Otsuka, K. Okamoto, and C. Itoi, Phys. Rev. B **78**, 184415 (2008).
[8] M. Lajkó, P. Sindzingre, and K. Penc, Phys. Rev. Lett. **108**, 017205 (2012).
[9] M. Sato, Phys. Rev. B **75**, 174407 (2007); M. Sato and T. Sakai, *ibid.* **75**, 014411 (2007).
[10] K. Okunishi, M. Sato, T. Sakai, K. Okamoto, and C. Itoi, Phys. Rev. B **85**, 054416 (2012).
[11] D. Charrier, S. Capponi, M. Oshikawa, and P. Pujol, Phys. Rev. B **82**, 075108 (2010).
[12] S. Nishimoto, Y. Fuji, and Y. Ohta, Phys. Rev. B **83**, 224425 (2011).
[13] Y. Fuji, S. Nishimoto, and Y. Ohta, J. Phys.: Conf. Ser. **400**, 032011 (2012).
[14] X. Plat, Y. Fuji, S. Capponi, and P. Pujol, Phys. Rev. B **91**, 064411 (2015).
[15] J. Schnack, H. Nojiri, P. Kögerler, G. J. T. Cooper, and L. Cronin, Phys. Rev. B **70**, 174420 (2004).
[16] N. B. Ivanov, J. Schnack, R. Schnalle, J. Richter, P. Kögerler, G. N. Newton, L. Cronin, Y. Oshima, and H. Nojiri, Phys. Rev. Lett. **105**, 037206 (2010).
[17] D. Babel and G. Knoke, Z. Anorg. Allg. Chem. **442**, 151 (1978).
[18] H. Manaka, Y. Hirai, Y. Hachigo, M. Mitsunaga, M. ito, and N. Terada, J. Phys. Soc. Jpn. **78**, 093701 (2009).
[19] H. Manaka, T. Etoh, Y. Honda, N. Iwashita, K. Ogata, N. Terada, T. Hisamatsu, M. Ito, Y. Narumi, A. Kondo, K. Kindo, and Y. Miura, J. Phys. Soc. Jpn. **80**, 084714 (2011).
[20] H. Manaka and Y. Miura, J. Phys.: Conf. Ser. **400**, 032049 (2012).
[21] H. Manaka and Y. Miura, J. Korean Phys. Soc. **62**, 2032 (2013).
[22] T. Masuda, M. Hagihara, and H. Manaka (private communication).
[23] H. Ishikawa, T. Okubo, Y. Okamoto, and Z. Hiroi, J. Phys. Soc. Jpn. **83**, 043703 (2014).
[24] J.-C. Domenge, P. Sindzingre, C. Lhuillier, and L. Pierre, Phys. Rev. B **72**, 024433 (2005).
[25] J.-C. Domenge, C. Lhuillier, L. Messio, L. Pierre, and P. Viot, Phys. Rev. B **77**, 172413 (2008).
[26] L. Messio, C. Lhuillier, and G. Misguich, Phys. Rev. B **83**, 184401 (2011). Note that the cuboc structure in the present paper corresponds to "Cuboc2" in this reference.
[27] H.-J. Koo, J. Magn. Magn. Mater. **324**, 2806 (2012).
[28] U. Wolff, Phys. Rev. Lett. **62**, 361 (1989).
[29] K. Hukushima and K. Nemoto, J. Phys. Soc. Jpn. **65**, 1604 (1996).
[30] S. Miyashita and H. Shiba, J. Phys. Soc. Jpn. **53**, 1145 (1984).
[31] K. Binder, Phys. Rev. Lett. **47**, 693 (1981).
[32] K. Harada, Phys. Rev. E **84**, 056704 (2011).
[33] H. Kawamura, J. Phys. Soc. Jpn. **54**, 3220 (1985); **61**, 1299 (1992).
[34] A. Mailhot, M. L. Plumer, and A. Caillé, Phys. Rev. B **50**, 6854 (1994).
[35] H. Kawamura, J. Phys.: Condens. Matter **10**, 4707 (1998).
[36] H. Kawamura, Can. J. Phys. **79**, 1447 (2001).
[37] H. Kawamura, Phys. Rev. B **38**, 4916 (1988).
[38] H. Kawamura, J. Phys. Soc. Jpn. **59**, 2305 (1990).
[39] J. C. Le Guillou and J. Zinn-Justin, Phys. Rev. B **21**, 3976 (1980).
[40] C. Holm and W. Janke, Phys. Rev. B **48**, 936 (1993).
[41] M. Campostrini, M. Hasenbusch, A. Pelissetto, P. Rossi, and E. Vicari, Phys. Rev. B **65**, 144520 (2002).
[42] A. Pelissetto and E. Vicari, Phys. Rep. **368**, 549 (2002).
[43] I. Dzyaloshinsky, J. Phys. Chem. Solids **4**, 241 (1958).
[44] T. Moriya, Phys. Rev. **120**, 91 (1960).
[45] B. Fåk, E. Kermarrec, L. Messio, B. Bernu, C. Lhuillier, F. Bert, P. Mendels, B. Koteswararao, F. Bouquet, J. Ollivier, A. D. Hillier, A. Amato, R. H. Colman, and A. S. Wills, Phys. Rev. Lett. **109**, 037208 (2012).
[46] O. Janson, J. Richter, and H. Rosner, Phys. Rev. Lett. **101**, 106403 (2008).
[47] O. Janson, J. Richter, and H. Rosner, J. Phys.: Conf. Ser. **145**, 012008 (2009).
[48] R. Suttner, C. Platt, J. Reuther, and R. Thomale, Phys. Rev. B **89**, 020408 (2014).
[49] S. Bieri, L. Messio, B. Bernu, and C. Lhuillier, arXiv:1411.1622.